Int. J. Heat Mass Transfer. Vol. 27, No. 4, pp. 587–598, 1984
Printed in Great Britain

0017–9310/84 $3.00 + 0.00

FREE CONVECTION OF GASES IN A HORIZONTAL CYLINDER WITH DIFFERENTIALLY HEATED END WALLS

G. H. SCHIROKY* and F. ROSENBERGER
Departments of Physics, and Materials Science and Engineering, University of Utah, Salt Lake City, UT 84112, U.S.A.

(*Received* 29 *September* 1982 *and in revised form* 11 *July* 1983)

Abstract—The free convective flow of gases in a horizontal cylinder (radius to length, $r_0/L = 0.1$) with different end temperatures and a linear temperature gradient at the wall was characterized by laser Doppler anemometry. Experiments were conducted over a wide range of Rayleigh numbers ($74 < Ra < 1.3 \times 10^6$, with $Ra \propto r_0^3$), which were varied via gas species and gas pressure. In the vertical mid-plane the velocity profiles in the cylinder core region at low Ra and in the end regions at high Ra were as expected from 2-D models. For the end regions, however, pronounced 3-D flow behavior was observed. It was found that only part of the fluid flows along the cold (hot) thermode into the lower (upper) half of the cylinder. The remaining part changes the flow direction by dropping (rising) at the side wall over a considerable distance from the respective thermode.

NOMENCLATURE

B	constant, dimensionless, equation (6)
C	Gill's free constant, dimensionless
c_p	specific heat [J g^{-1} K^{-1}]
f	Doppler frequency [s^{-1}]
g	gravitational acceleration [m s^{-2}]
h	height of rectangular enclosure [m]
k	fluid thermal conductivity [W m^{-1} K^{-1}]
k_1	nondimensional axial temperature gradient in cylinder core region
k_2	constant, dimensionless, equation (8)
L	length of cylinder [m]
m	constant, dimensionless, equation (17)
Pr	Prandtl number, ν/κ
Q_m	mass flow rate [g s^{-1}]
Q_v	volume flow rate [m^3 s^{-1}]
r	radial position [m]
r'	dimensionless radial position, r/r_0
r_0	radius of cylinder [m]
Ra	Rayleigh number, $\beta g \Delta T r_0^3/\nu\kappa$
s	width of momentum boundary layer [m]
T	temperature [K]
T'	dimensionless temperature, $(T - T_c)/(T_h - T_c)$
T_h	temperature of hot thermode [K]
T_c	temperature of cold thermode [K]
ΔT	$T_h - T_c$ [K]
v_x, v_y, v_z	velocity components in x-, y-, z-directions [m s^{-1}]
v'_x, v'_y, v'_z	dimensionless velocity components in x-, y-, z-directions, $v_x r_0/\kappa$, etc.
v_r, v_c	radial and circumferential velocity components [m s^{-1}]
v'_r, v'_c	dimensionless radial and circumferential velocity components, $v_r r_0/\kappa$, etc.
x, y, z	position components [m]
x', y', z'	dimensionless position components, x/r_0, etc.

Greek symbols

α	angle (Fig. 3)
β	coefficient of volumetric thermal expansion [K^{-1}]
η	viscosity [cP]
θ	angle (Fig. 1)
κ	fluid thermal diffusivity [m^2 s^{-1}]
λ	wavelength of laser light [m]
ν	kinematic viscosity [m^2 s^{-1}]
ρ	density of gas [g m^{-3}].

Subscripts

e	rectangular enclosure, equations (12) and (13)
max	maximum
0, I, II, III	order of term in solution to perturbation analysis.

Abbreviations

BLR	boundary layer regime
LDA	laser Doppler anemometry
SNR	signal-to-noise ratio.

1. INTRODUCTION

THE LITERATURE on convection in enclosures has been reviewed by Ostrach [1] and Catton [2]. A selection of more recent work is listed in Schiroky and Rosenberger [3]. Almost all numerical and experimental investigations deal with rectangular enclosures; only little is known about free convection in long horizontal cylinders with differentially heated end walls (thermodes). Insight into the flow characteristics in such geometries is important, e.g. for the solution of heat transfer problems [3] and for stress analysis in dead-leg pipes connected to hot main pipes [4]. Our motivation

* Present address: GA Technologies, P.O. Box 81608, San Diego, CA 92138, U.S.A.

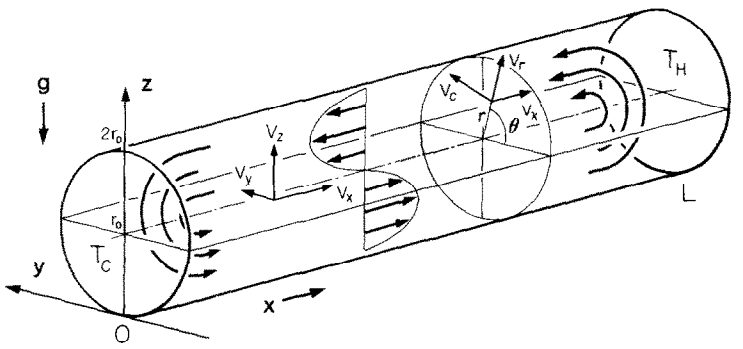

FIG. 1. Free convection in a cylinder with differentially heated end walls: fluid flow (schematic) and definition of location and velocity coordinates.

for this study was the need for a better understanding of convection in crystal growth by physical or chemical vapor transport in a cylindrical ampoule [5].

The general flow behavior in shallow rectangular enclosures and long cylinders is qualitatively similar. Warmer fluid rises near the hot thermode and flows in the upper half of the enclosure towards the cold end. There it reverses its direction and returns in the lower half to the hot end. This behavior is schematically shown in Fig. 1, which also serves as a definition sketch for the coordinates used in the following analyses.

In order to obtain analytical expressions for the velocity and temperature distribution in the core region of a long cylinder, Bejan and Tien [6] carried out a perturbation analysis. They assumed power series expressions in Ra for the nondimensional velocity components v_r', v_c', v_x' and temperature T' in the form

$$(v_r', v_c', v_x', T') = (v_r', v_c', v_x', T')_0 + (v_r', v_c', v_x', T')_I Ra + (v_r', v_c', v_x', T')_{II} Ra^2 + \cdots \quad (1)$$

They obtained $v_{x0}' = v_{xII}' = 0$, and thus for the axial velocity component

$$v_x' = v_{xI}' \, Ra = \tfrac{1}{8} \, Ra \, k_1 (r'^3 - r') \sin\theta, \quad (2)$$

where k_1 is the dimensionless axial temperature gradient in the core. In the limit $Ra \to 0, k_1 = r_0/L$, and for $Ra \to \infty, k_1 \to 0$.

Kimura and Bejan [7] treated the cylinder core flow as fully developed, i.e. they assumed zero axial velocity gradients and a constant axial temperature gradient. This considerably simplifies the governing equations. The numerical solutions obtained in ref. [7] for $Ra\, r_0/L = 10^2$ and 10^3, and $Pr = 6.78$, agree with the results of ref. [6].

Shih [8] also considered the flow in the middle portion of a cylindrical enclosure as being fully developed. He used a computer to extend Bejan and Tien's [6] three-term expansion for velocity and temperature distribution to 47th order in Ra, and obtained and analyzed a 24-term series in Ra^2 for the Nusselt number. Unfortunately he did not present analytical expressions for velocity and temperature.

An experimental study on free convection in a horizontal cylinder with different end temperatures was performed by Kimura and Bejan [9]. They observed the circulation of water in a Plexiglas cylinder (length $L = 124.5$ cm, radius $r_0 = 7.0$ cm) for an Ra-range of approximately 10^7–10^9. They also photographed streaklines generated with the pH-indicator method. This revealed a practically stagnant fluid in the mid-depth region and thin horizontal jets of fluid proceeding along the top and bottom of the cylinder towards opposite thermodes. However, their experimentally determined Nusselt numbers (Nu) deviate from predicted values by several orders of magnitude [6]. Good agreement with Kimura and Bejan's experimentally determined Nusselt numbers [9] was recently obtained in a simple boundary layer analysis by Schiroky and Rosenberger [3].

In this paper we present the results of our velocimetric work on free convection of gases in a differentially heated horizontal cylinder ($r_0 = 1.0$ cm, $L = 10.0$ cm). After a concise description of the experimental details in the next section we deal with the velocity profiles and flow rates in the core region. This is followed by a critical discussion of the validity range of the perturbation analysis for this problem and a comparison of our results with most recent 3-D calculations of the core flow. Then the complex 3-D features of the flow reversal near the thermodes are presented and, for the high Ra range, compared with boundary layer predictions.

2. EXPERIMENTAL APPARATUS AND TECHNIQUES

Laser velocimetry was chosen as a noninvasive flow measurement technique to precisely determine velocity components. The cylindrical glass enclosure was optically completely accessible. The variation of Ra over several orders of magnitude was achieved by varying gas pressure and composition while ΔT was held constant.

2.1. *Design of the cylindrical enclosure*

The cylindrical quartz-glass enclosure is schematically shown in Fig. 2. An outer glass tube (35 mm O.D.) was fused to a longer inner glass tube (20 mm I.D.). The

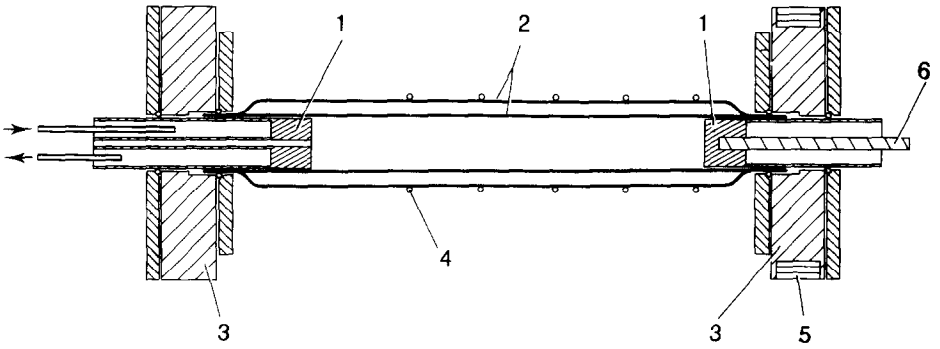

FIG. 2. Cross-section of cylindrical convection cell: (1) thermostated copper thermodes; (2) concentric quartz glass tubes, interspace evacuated and sealed; (3) brass supports with O-ring fittings; (4) (radiation) heating loops; (5) heating tape; (6) heating cartridge.

volume between both tubes was evacuated and then sealed off to minimize the influence of external convection. The glass construction was held in place with standard O-ring fittings on brass mounting blocks. Two pistons (stainless steel tubes with copper end pieces), closely fitted into the inner tube, served as thermodes. One piston was water-cooled ($T_c = 27°C$), the other one heated ($T_h = 89°C$) with a built-in soldering iron heating element. The mounting block at the hot side was also heated to T_h with a heating tape. A linear temperature gradient on the inner tube wall was obtained from five individually controlled loop heaters (wire diameter 0.1 mm, resistivity 0.4 Ω cm^{-1}) that were closely tied to the outer tube. The temperature distribution on the innermost wall was measured under vacuum with a springloaded thermocouple and the currents through the loop heaters were adjusted until a linear temperature profile was established. Deviations from a straight line connecting T_h and T_c and from cylindrical symmetry were not larger than 1°C. For the flow studies, the thermocouple was removed and the feedthrough closed. The temperature profile was checked periodically for linearity, and the currents were readjusted if necessary.

All temperatures were held constant to $\pm$ 0.1°C. The ratio of the thermal conductivities of quartz-glass and nitrogen is about 50 at room temperature. Hence, we regard the glass wall as 'conducting'.

2.2. *The LDA-system*

A schematic representation of the dual beam LDA-system used in the forward scattering mode is shown in Fig. 3. The interference of the wavefronts of the two coherent laser beams creates a fringe pattern at the beam crossing. The crossing region, or probe volume, has approximately the shape of an ellipsoid with a length of 0.45 mm and a diameter of 0.09 mm. With a fringe spacing of about 1.7 μm there are roughly 50 fringes present. A particle ('seed'), passing through the probe volume, scatters light periodically, say with a frequency f. This light is collected by a lens focused at the beam crossing. An aperture is used to allow only light scattered within the probe volume to reach the photomultiplier. There it is converted to an electrical signal, which after passing through a high-pass filter, is processed in a spectrum analyzer. The particle velocity component perpendicular to the fringes, e.g. v_x, is related to f via

$$f = 2v_x \sin(\alpha/2)/\lambda. \tag{3}$$

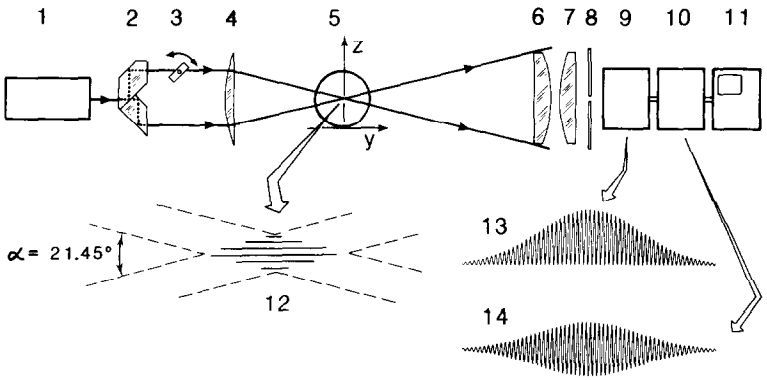

FIG. 3. Schematic of LDA-system: (1) He–Ne laser, 15 mW; (2) beam splitter; (3) scanning glass plate for frequency shifting; (4) focusing lens, focal length = 120 mm; (5) cylindrical enclosure, viewed axially; (6) collecting lens, focal length = 250 mm; (7) scattered light focusing lens; (8) aperture; (9) photomultiplier; (10) high-pass filter; (11) frequency analyzer; (12) enlarged interference fringes; (13) optical signal received by photomultiplier (intensity vs time); (14) electrical signal leaving high-pass filter (voltage vs time).

The laser beams have a Gaussian intensity distribution, which leads to a higher fringe contrast in the central region of the probe volume. Hence, the photomultiplier receives an optical signal, as indicated in Fig. 3, with a high frequency component (Doppler frequency) and a low frequency component (pedestal signal) corresponding to the intensity envelope [10]. The ratio of Doppler to pedestal signal determines the signal quality. Obviously one will try to separate both components by filtering. However, at very low frequencies it becomes increasingly difficult to determine the frequency cut-off of the high-pass filter. Due to the finite roll-off, lower frequency Doppler signals may then be attenuated. In our study the measurement of very low velocities was crucial. Hence, we applied a light-frequency shifting technique which increased the Doppler frequencies without altering the pedestal signal frequency. This is accomplished by passing one of the beams through an oscillating parallel glass plate, thus modulating the effective optical path length of that beam. This scanner plate, as indicated in Fig. 3, is mounted on a shaft that rotates at a linear rate approximately $\pm 2°$ from a 45° angle to the beam. A sawtooth signal with a ratio of ramp time to fall time equal to 19 applied to the driving solenoid makes the plate continuously sweep and snap back to its starting position. The resulting continuous phase shifting between the two beams causes the fringe pattern to move in one direction and then return to the starting position at a 19 times faster rate. When seeds and fringes move in opposite directions, a higher Doppler frequency results. Thus, we were able to measure velocities as low as 0.1 mm s^{-1}. When seeds and fringes move in the same direction, the Doppler frequency is reduced as compared to the signal obtained with a stationary scanner plate. The sign of the frequency shift allows for determination of the sign of the observed flow vector component.

For a more detailed discussion of laser velocimetry the reader is referred to the literature, e.g. refs. [10–13].

As we have indicated above, LDA experiments require seeds. Rayleigh scattering of molecules (with a typical cross-section of 10^{-33} m^2) is insufficient for an adequate signal-to-noise ratio (SNR). However, a large SNR can be obtained from micrometer-size particles (scattering cross-section of order 10^{-12} m^2), i.e. through Mie scattering. According to Drain [11], the ratio of particle diameter to fringe spacing should be less than or equal to 0.6, where 0.6 offers ideal conditions. Thus, for our case the seed diameter should be less than or equal to 1 μm.

We found cigarette smoke to be a very suitable seeding-medium. The size distribution for tobacco smoke lies between 0.1 and 1.0 μm [10, 14]. In order to test whether the particle velocities obtained by LDA represent actual fluid flow velocities, we measured at fixed locations in the cylinder the velocity for up to 3 h after the cigarette smoke had been introduced. Within such long time spans the smoke concentration had considerably decreased by deposition of seeds on the walls, and the size distribution had most likely shifted towards larger sizes [14]. Yet, the velocities never changed more than a few percent. A detailed discussion on the ability of particles to follow a certain fluid flow is given in ref. [10], indicating that in our flow configuration seed and fluid velocities should be essentially identical.

The seeding procedure itself was simple. After evacuation, the cylinder was filled with nitrogen to atmospheric pressure. The filter of a cigarette was joined with a rubber hose to one end of a U-tube suspended in a dewar filled with liquid nitrogen. The other end of the U-tube extended through the feedthrough in the cold thermode into the cylinder. Creation of a small underpressure in the cylinder caused the cigarette to be smoked through its own filter and the U-tube, where undesirable vapors (H_2O, CO_2, etc.) were frozen out. Thus, practically pure nitrogen, containing smoke, was introduced into the cylinder, essentially retaining the composition of the fill gas. Upon completion of the seeding, the 'smoke pipe' was removed, a copper rod was inserted flush with the inner wall of the thermode and the cylinder's pressure adjusted to the desired value.

We have measured the three velocity components v_x, v_y and v_z on various grid locations that span most of the cylinder's volume. The arrangement for the measurement of v_z is indicated in Fig. 3. A 90° rotation of the beam splitter around the y-axis allowed for a measurement of v_x. To determine v_y, the laser was suspended from the ceiling, the two beams lying in a y–z plane. Velocities greater than 1 mm s^{-1} were measured with a resolution of $\pm 1\%$, and of 0.1 mm s^{-1} with $\pm 10\%$. During the course of the experiments certain 'standard' velocity profiles were periodically redetermined. The standard deviation was found to be less than $\pm 10\%$.

For changes of the measurement location, the cylinder was moved with respect to the probe volume with a dial gauge accuracy of ± 0.01 mm in all three coordinate directions. When the laser beams, in the y–z plane, crossed exactly on the cylinder axis, all reflection spots on the tube wall disappeared. This was used as a convenient positioning reference in the y- and z-directions. For off-axis positions of the probe, the aberrations due to refraction in the glass wall were computationally corrected for. Accurate positioning with respect to the cold thermode was obtained from extrapolations of the velocity profiles of Section 3.3 to zero 'at $x = 0$'. (Note that due to the finite probe volume some averaging in the velocity is unavoidable.) Based on these procedures and corrections, the resolution for the measurements locations was between 0.1 and 0.2 mm. Both v_y and v_z could be measured to within that distance from a thermode. For the v_x-component, however, the closest position of a cross-sectional plane (x = const.) with respect to a thermode was limited to 3 mm (i.e. $x = 3$ or 97 mm) due to interference of the thermode with one of the beams.

Table 1

Experiment	Gas and p [10^5 Pa]	ρ [g l^{-1}]	η [cP]	k [W cm^{-1} K^{-1}]	c_p [J g^{-1} K^{-1}]	ν [cm^2 s^{-1}]	κ [cm^2 s^{-1}]	Pr	Ra
1	0.133 N_2	0.146	0.01968	2.80×10^{-4}	1.036	1.35	1.85	0.73	74
2	0.400 N_2	0.437	0.01968	2.80×10^{-4}	1.036	0.450	0.619	0.73	660
3	0.667 N_2	0.728	0.01968	2.80×10^{-4}	1.036	0.270	0.372	0.73	1830
4	0.933 N_2	1.019	0.01968	2.80×10^{-4}	1.036	0.193	0.265	0.73	3580
5	1.200 N_2	1.310	0.01968	2.80×10^{-4}	1.036	0.150	0.206	0.73	5920
6	1.467 N_2	1.602	0.01968	2.80×10^{-4}	1.036	0.123	0.169	0.73	8860
7	2.133 N_2	2.329	0.01968	2.80×10^{-4}	1.036	0.0845	0.116	0.73	18 700
8	0.933 N_2 0.533 SF_6	3.849	0.0192	2.13×10^{-4}	0.766	0.0499	0.0729	0.68	50 880
9	0.933 N_2 0.933 SF_6	5.972	0.0187	1.97×10^{-4}	0.732	0.0313	0.0451	0.69	130 500
10	0.533 N_2 1.600 SF_6	9.072	0.0179	1.72×10^{-4}	0.695	0.0197	0.0272	0.72	342 100
11	0.533 N_2 1.600 C_4F_8	12.832	0.0143	1.30×10^{-4}	0.787	0.0111	0.0129	0.86	1 283 000

2.3. *Conditions for measurements at different Rayleigh numbers*

The thermode temperatures $T_c = 27°C$, and $T_h = 89°C$, were held constant for all measurements. Different Ra's were established by varying the nitrogen gas pressure, and by adding gases with high molecular weights into the cylinder. Those were sulfurhexafluoride (SF_6) and octafluorocyclobutane (C_4F_8), which are noncorrosive, nontoxic, and thermally stable. The specific conditions under which the measurements were performed are listed in Table 1.

In the pressure range considered here, β, c_p, η, and k of a gas are practically pressure-independent. Then, as ΔT is kept constant, for monocomponent gases

$$Ra \sim \rho^2. \tag{4}$$

Ignoring the variations of c_p, η and k of different gases, relation (4) can be used for rough estimates of Ra. The advantage of heavy gases like SF_6 and C_4F_8 is then obvious. For instance, the Ra of experiment 11 (Table 1) would have required a pure nitrogen pressure of 17.6×10^5 Pa which far exceeded the pressure limitation of our experimental setup.

The physical constants ρ, η, k, and c_p of the gases used were taken from ref. [15]. The Sutherland equation [16] was used to evaluate k and η at $T = 0.5(T_h + T_c)$. For the gas mixtures used in experiments 8–11, k and η of the mixtures were evaluated with a method described in ref. [17]. For β we took $2(T_h + T_c)^{-1}$. The density ρ was calculated from the measured pressure assuming ideal gas behavior.

3. RESULTS AND DISCUSSION

At all Ra's we observed a centrosymmetric flow behavior as schematically shown in Fig. 1. We will first take a closer look at the measured core flow and compare it with theoretical predictions. Then we will focus on distinct features of the flow near the cold thermode. Due to the centrosymmetry the same results with opposite sign apply near the hot end.

3.1. *The core flow*

The axial velocity component v_x was measured as a function of the z-coordinate in the vertical mid-plane ($y = 0$) at half-length ($x = 50.0$ mm). S-shaped velocity profiles were obtained that we will refer to as 'S-curves'. The results are shown in Fig. 4. The magnitude of the velocity maxima initially increased with Ra, but then dropped again. The physical origin of this drop lies in our Ra adjustment via ρ and will be discussed below. Also, the location of the maxima shifted closer towards the wall with increasing Ra.

To gain insight into the physical nature of the S-curve, we extended Bejan and Tien's [6] perturbation analysis by one order in Ra and obtained an expression for $v'_{x\mathrm{III}}$ (for details see ref. [18])

$$v'_{x\mathrm{III}} = B\sin\theta\left(-\frac{143}{1680}r'^{11}+\frac{3}{4}r'^{9}-\frac{21}{10}r'^{7}+\frac{125}{48}r'^{5}-\frac{201}{140}r'^{3}+\frac{4}{15}r'\right)+4B\sin^3\theta\left(\frac{1}{112}r'^{11}-\frac{1}{24}r'^{9}+\frac{3}{40}r'^{7}-\frac{1}{16}r'^{5}+\frac{17}{840}r'^{3}\right), \tag{5}$$

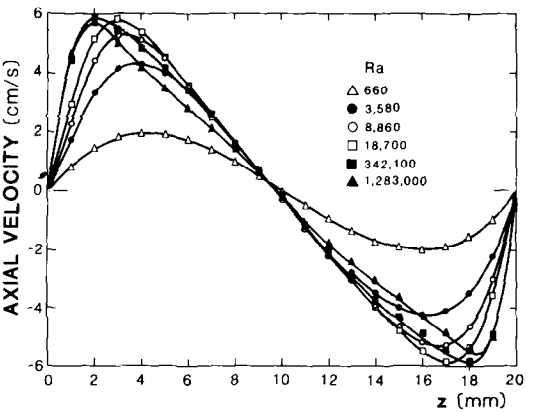

FIG. 4. Axial velocity component in vertical mid-plane ($y = 0$) at $x = 0.5L$ for experiments 2, 4, 6, 7, 10, and 11.

where

$$B = \frac{k_1^3}{1\,474\,560 Pr}. \tag{6}$$

Now

$$v'_x = v'_{x\mathrm{I}}\, Ra + v'_{x\mathrm{III}}\, Ra^3. \tag{7}$$

Figure 5 presents plots of $v'_{x\mathrm{I}}\, Ra$ and $v'_{x\mathrm{III}}\, Ra^3$ vs r' for the case of $Ra = 20\,000$, $Pr = 0.73$, and $\theta = \pi/2$. We see that $v'_{x\mathrm{III}}\, Ra^3$ forms a counterflow contribution to the first order S-profile. For considerably higher Ra, $v'_{x\mathrm{III}}\, Ra^3 \gg v'_{x\mathrm{I}}\, Ra$, and thus only the counterflow would remain if the series expansion is terminated in third order of Ra. This is a rather nonphysical prediction which suggests that, once $v'_{x\mathrm{I}}\, Ra$ and $v'_{x\mathrm{III}}\, Ra^3$ become comparable in magnitude, the evaluation of higher order terms becomes essential. However, this would not be meaningful as the perturbation analysis *per se* is limited to low Ra, which can be shown as follows. The zero-order component of T' is given as [6]

$$T'_0 = k_1 x' + k_2. \tag{8}$$

Evaluation of higher order components of T' shows, that for all orders in Ra,

$$\frac{\partial T'}{\partial x'} = k_1, \tag{9}$$

irrespective of r'. However, in the case of a conducting wall, we have the boundary condition

$$\left.\frac{\partial T'}{\partial x'}\right|_{r'=1} = r_0/L. \tag{10}$$

Thus, from equations (9) and (10), it becomes clear that the perturbation analysis is reasonably valid only as long as $k_1 \approx r_0/L$. This, as we have shown elsewhere (for the aspect ratio under consideration), is the case up to $Ra \approx 500$ [18]. For $Ra = 10\,000$, $k_1 = 0.5 r_0/L$, which might, somewhat arbitrarily, be taken as the upper limit at which the analysis yields reasonable predictions. Considering this physical limitation, an evaluation of higher order terms of v'_x appears as a rather futile exercise.

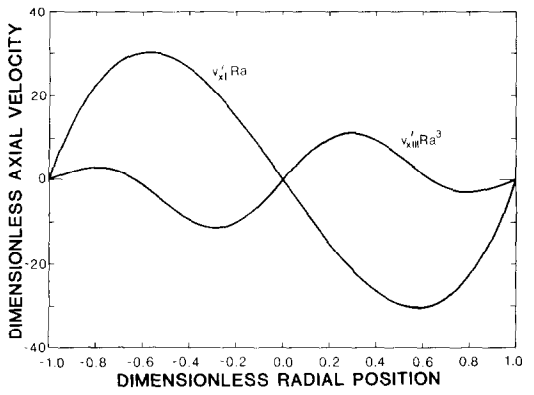

FIG. 5. The terms $v'_{x\mathrm{I}}\, Ra$ and $v'_{x\mathrm{III}}\, Ra^3$ in the solution to the perturbation analysis [equation (7)] for $Ra = 20\,000$, $Pr = 0.73$, and $\theta = \pi/2$.

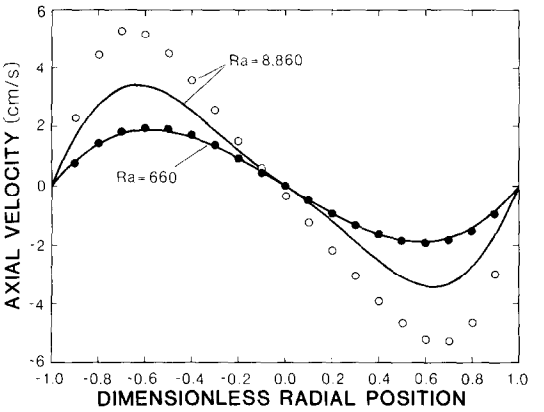

FIG. 6. Velocity profiles for $Ra = 660$ and 8860: points, measured; solid curves, computed from equation (7).

Relation (7), evaluated for $Ra = 660$ and 8859, is plotted together with the experimental data in Fig. 6. For the lower Ra, experiment and theory agree very well, while for the higher Ra equation (7) underestimates the actual flow velocities. From Fig. 6 it becomes evident that the calculation of $v'_{x\mathrm{III}}$ was useful, as the model now predicts the shift of the velocity maximum towards the wall, i.e. towards higher r'-values. This tendency could not be seen from the simpler relation (2). Note that equations (5)–(7) indicate that high Pr fluids should exhibit this shift at higher Ra.

Now, in spite of the limitations of the perturbation analysis, it is interesting to see to what extent it can be used for rough estimates of maximum flow velocities at very high Ra. Based on the grossly simplifying assumption, that for any Ra the S-profile is given by equation (2), one can write for the maximum in the S-profile

$$v'_{x,\max} = 0.0481 Ra\, k_1. \tag{11}$$

This relation is shown in two forms in Fig. 7 together with the experimentally determined S-curve maxima, in a double-logarithmic plot. For Curve 1, we set $k_1 = r_0/L$, while for Curve 2, k_1 was obtained from an

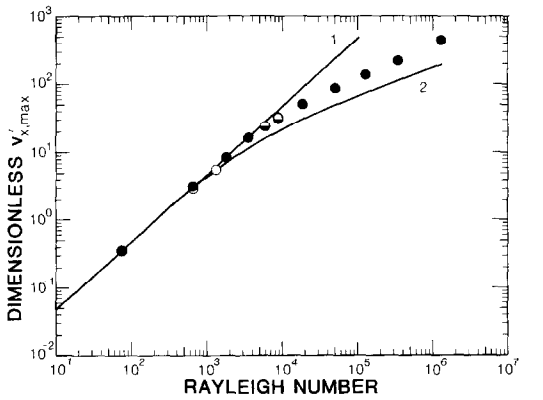

FIG. 7. Maxima of nondimensional velocity in S-curve vs Ra for experiments 1–11 (full circles); numerical values (open circles) [19], solid curves computed from equation (11), where in Curve 1: $k_1 = r_0/L$, and in Curve 2: k_1 from ref. [18].

end-integral analysis [18]. Also shown are numerically determined S-curve maxima of Roux [19], which are in excellent agreement with the experimental findings.

The underestimation of the actual $v'_{x,\max}$ values by Curve 2 can be understood following arguments of Cormack *et al.* [20, 21] and Imberger [22]. These authors studied theoretically and experimentally convection in shallow 2-D cavities. They derived for the horizontal core velocity an expression similar to equation (2), i.e. the velocity is proportional to the horizontal temperature gradient k_1, and its distribution over the cavity height is S-shaped. On numerical evaluation of k_1 and insertion into their expression, they noted that for high Ra actual flow velocities were higher than the ones predicted. Their explanation of this discrepancy holds as well for convection in a cylindrical enclosure. At small Ra, the horizontal temperature gradient comprises the only driving force for fluid motion. At high Ra, boundary layers form at the vertical end walls, and fluid entrainment–detrainment from the boundary layers becomes the controlling driving force. Therefore, equation (11) increasingly underestimates the actual horizontal flow velocities, as it is based entirely on the core-gradient mechanism, neglecting any contributions from the end zones.

Figure 7 shows that the dimensionless $v'_{x,\max}$ steadily increases with Ra. The actual maximum flow velocity in our experiments, however, decreases at very high Ra's, as depicted in Fig. 4. This decrease is a consequence of our Ra adjustment via ρ, rather than ΔT. To show this we can use, for instance, Bejan and Tien's 2-D analysis of natural convection heat transfer in a rectangular horizontal cavity with different end temperatures [23]. They derived for the high Ra range, i.e. for the boundary layer regime, a relation for the nondimensional horizontal temperature gradient k_{1e}

$$k_{1e} = 60.93 Ra_e^{-3/5}, \tag{12}$$

where the subscript e denotes the rectangular enclosure. Since $v'_{xe} \sim Ra_e k_{1e}$, with equation (12), $v'_{xe} \sim Ra_e^{2/5}$. Using equation (4) it follows that

$$v'_{xe} \sim \rho^{-1/5}. \tag{13}$$

Thus, in the boundary layer regime, a tenfold increase of the gas pressure which corresponds to a 100-times higher Ra, is expected to reduce core flow velocities by a factor of 0.63. It should be noted, however, that equation (12) and, hence, equation (13) are based on the core-gradient mechanism only and also neglect changes in the shape of the v'_{xe}-profile with Ra, e.g. a radial shift of the location of the maximum.

3.2. *Volume and mass flow rates*

We have calculated volume and mass flow rates, Q_v and Q_m by integrating the measured velocity distributions at $x = L/2$ over the (upper) half circular cross-section in the form

$$Q_v = \int v_x \, dA, \tag{14}$$

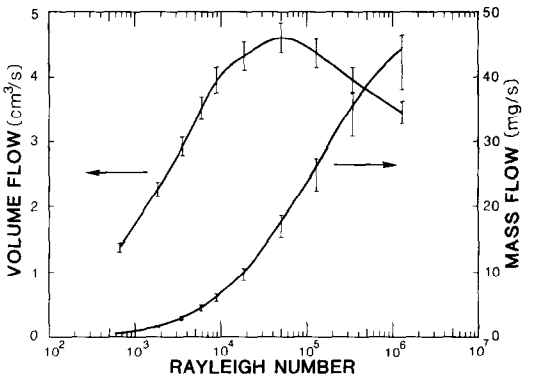

FIG. 8. Mass and volume flow rates at $x = 0.5L$ vs Ra for experiments 2–11.

and

$$Q_m = \int \rho v_x \, dA. \tag{15}$$

The integration was based on data obtained for a uniform grid of 1 mm spacing in the y- and z-directions. The density in equation (15) was taken at $0.5(T_h + T_c)$. The results are plotted as a function of Ra in Fig. 8. The error bars reflect the uncertainty resulting from the numerical integration procedure and from the estimation of the density. As expected, Q_m steadily increases with Ra. The decrease in Q_v at high Ra will be analyzed in the next section.

3.3. *The vertical velocity component near the cold end wall in the plane* $y = 0$

The vertical velocity component v_z was measured along the cylinder axis near the cold end wall for various Ra's. The observed profiles are shown in Fig. 9. The thickness of the momentum boundary layer decreases steadily with Ra. The maximum in the vertical velocity initially increases with Ra and then becomes approximately constant.

The boundary layer flow along the differentially heated vertical walls of tall rectangular 2-D enclosures has been treated in a classical paper by Gill [24]. Roux *et al.* [25], and Marshall *et al.* [26] showed numerically,

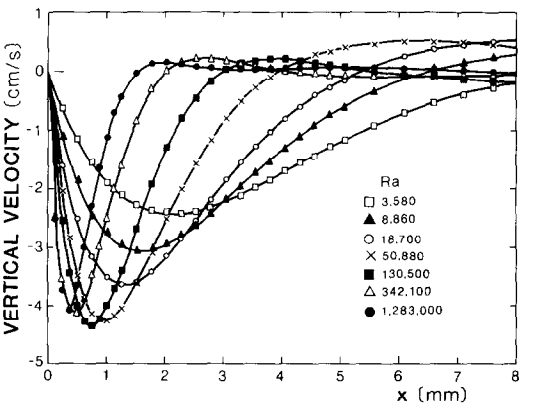

FIG. 9. Vertical velocity component v_z vs x on cylinder axis for experiments 4 and 6–11.

that this theory can also be applied to the case of a square cavity. More recently, Simpkins and Dudderar [27] experimentally confirmed Gill's prediction for a wide, shallow, rectangular enclosure with a height to length ratio of 0.25. Since the convective fluid flow in the vertical mid-plane ($y = 0$) of the cylinder must be two-dimensional ($v_x \neq 0$, $v_y = 0$, $v_z \neq 0$), it is reasonable to test Gill's theory for the cylindrical enclosure.

Based on a particularly revealing formulation of Gill's results by Roux *et al.* [25], v_z' along the cylinder-axis near the cold end can be written as

$$v_z' = -\sqrt{2}\sqrt{Ra}\, C^2 \exp(-mx/r) \sin(mx/r), \quad (16)$$

with

$$m = \frac{0.42}{C} Ra^{0.25}. \quad (17)$$

Gill's free constant C was evaluated by several authors [24, 25, 28, 29]. Roux *et al.* [25], with a highly accurate numerical method, obtained $C = 0.80$ for a square cavity. A plot of our experimental $v'_{z,\max}$-values vs $\sqrt{Ra}$ yields $C = 0.69$. From equations (16) and (17), the maximum of v_z' and its location s, should follow $v'_{z,\max} \sim Ra^{0.50}$, $s \sim Ra^{-0.25}$. Experimentally we found for the four highest Ra's that $v'_{z,\max} \sim Ra^{0.52}$, $s \sim Ra^{-0.32}$. Figure 10 shows the good agreement between predicted [equations (16) and (17)] and experimentally determined velocity profiles for the two Ra's that bound the range considered. Thus, the applicability of Gill's theory to the horizontal cylinder at high Ra is confirmed within experimental accuracy. At this point, this does not appear very surprising, since in our system as well as in Gill's model the width of the momentum boundary layer is small as compared to the height (diameter) of the vertical wall (thermode). In the following sections, however, we will encounter 3-D flow features that make the validity of Gill's analysis for our case somewhat astounding.

The above comparison between theory and experiment reveals that the boundary layers at the vertical thermodes are fully developed at $Ra \geqslant 50\,000$. We will refer to this Ra-range as the boundary layer regime (BLR). With equations (4) and (16), and with $v_z = v_z'\kappa/r_0$, one obtains for the BLR that for fixed ΔT, $v_{z,\max}$ is independent of Ra, and proportional to $Pr^{-0.5}$. Thus, the small decrease of $v_{z,\max}$ with Ra (Fig. 9) in the BLR can be interpreted in terms of the slightly increased Pr of the gases used to establish higher Ra's (Table 1).

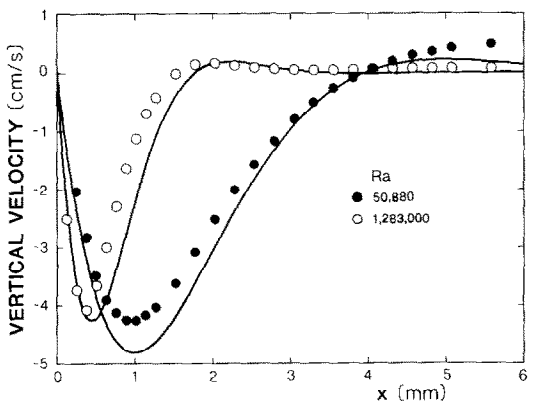

FIG. 10. Vertical velocity component v_z vs x on cylinder axis for $Ra = 50\,880$ and $1\,283\,000$: points, measured; curves, computed from equation (16).

Since in the BLR, $v_{z,\max}$ stays approximately constant and the velocity boundary layer width decreases with Ra (Fig. 9) it follows that the volume flow rate in the boundary layer in the plane $y = 0$ decreases with Ra. Above we presented volume flow rates in the core region, and showed the decrease of Q_v at high Ra in Fig. 8. This reveals a rather interesting result: the onset of the BLR can be found by measuring Q_v in the core as a function of Ra. The critical value is approximately given by the Ra for which $dQ_v/dRa = 0$, Fig. 8. Thus the lower limit for the validity of Gill's theory for the end zones can be obtained from information about the flow in the cylinder core. This is of particular interest for configurations with limited (optical) access to the end regions.

3.4. *The momentum boundary layer at the cold thermode*

The extent of the velocity boundary layer along the cylinder axis was discussed in detail in the previous section. In order to determine the overall shape of the boundary layer, we measured v_z on lines parallel to the cylinder axis with y- and z-spacings of 1 mm. Surfaces for the location of $v_{z,\max}$ for different Ra's are presented for the cold end region in Fig. 11. One sees that this boundary layer surface approximates an inclined plane. For the whole range covered in this sequence ($660 \leqslant Ra \leqslant 342\,100$), $x(v_{z,\max})$ varied roughly linearly from 0.5 to 1.5 s for $2r_0 \geqslant z \geqslant 0$, with only weak dependence on y. Since, as shown in Section 3.3, s can be readily predicted, this result facilitates simple, yet reasonably accurate estimates of heat and mass fluxes between the end walls. Elsewhere [3] we have utilized this insight for the calculation of Nusselt numbers in good agreement with earlier experiments.

3.5. *The flow reversal near the cold end in the plane* $y = 0$

To further characterize the flow in the end zones, we measured the velocity components v_x and v_z at different x- and z-locations in the plane $y = 0$ near the cold end. The results for $Ra = 3580$ and $1\,283\,000$ are depicted in Fig. 12. For the lower Ra [Fig. 12(a)] the v_x-component profile stayed S-shaped in the region of flow reversal. For the highest Ra [Fig. 12(b)] the maximum in the S-profile had moved close to the wall; throughout the end zone the highest v_x-values were measured at $z = 1$ and 19 mm, respectively. This shows well the transition to the horizontal boundary layer flow. In Fig. 12(b) one can follow the spatial development of this boundary layer after flow reversal.

Two more features can be deduced from Fig. 12: the development of a recirculation flow in the end region and a skewness of the overall convection roll.

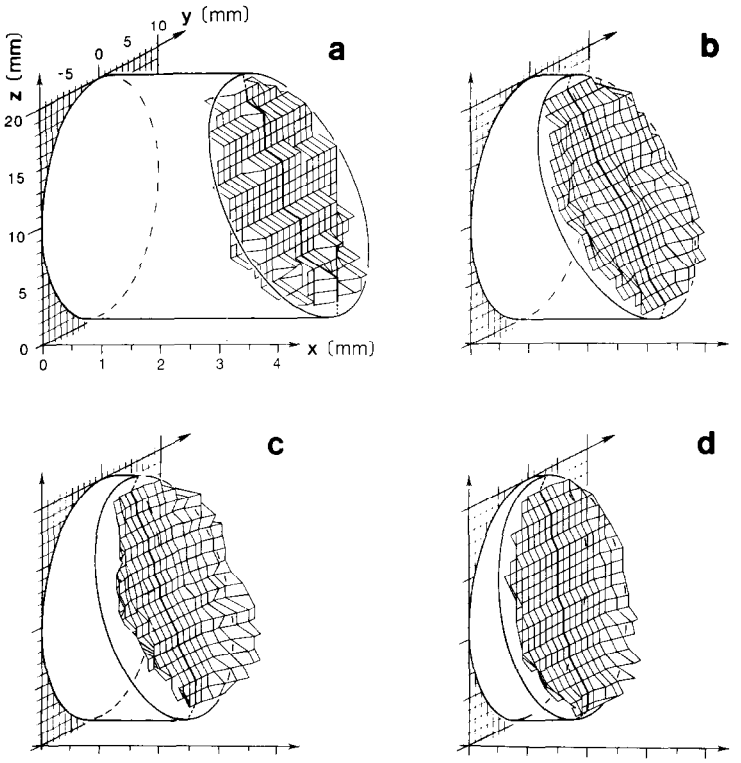

FIG. 11. Velocity boundary layer (location of v_z-maxima) at cold end wall for various Ra's. (a) $Ra = 660$; (b) $Ra = 18\,700$; (c) $Ra = 50\,880$; (d) $Ra = 342\,100$. Each ellipse contains least square fit through points in the $y = 0$ plane (see heavy line) of the respective figure.

At $Ra = 3580$ [Fig. 12(a)] shear instability caused fluid recirculation about $v_x = 0$ at $z \approx 10.5$ mm. This inclination increases with Ra as measurements at $Ra = 8860$ and 18 700 showed. This tendency is also reflected in the increasingly higher positive v_z-values in Fig. 9. At $Ra = 1\,283\,000$ [Fig. 12(b)] an additional recirculation cell had developed in the lower left corner. The skewness of the overall flow roll had increased such that $v_x = 0$ occurred at $z \approx 12.5$ mm. Similar increases in inclination of the convection roll with Ra were found in a wide rectangular enclosure with $h/L = 0.2$ by Ostrach *et al.* [30].

A critical evaluation of Fig. 12 with respect to continuity leads to a very important result. One sees that the v_x-component (at fixed z) decreases considerably before flow reversal occurs near the end

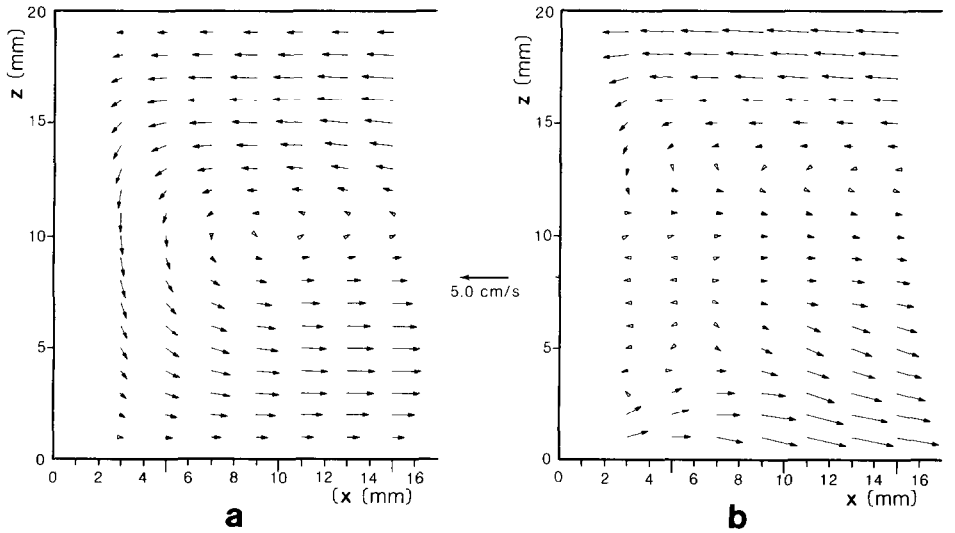

FIG. 12. v_x–v_z velocity field near cold thermode in vertical mid-plane ($y = 0$) for (a) $Ra = 3580$ and (b) $Ra = 1\,283\,000$. Same velocity scale for both figures.

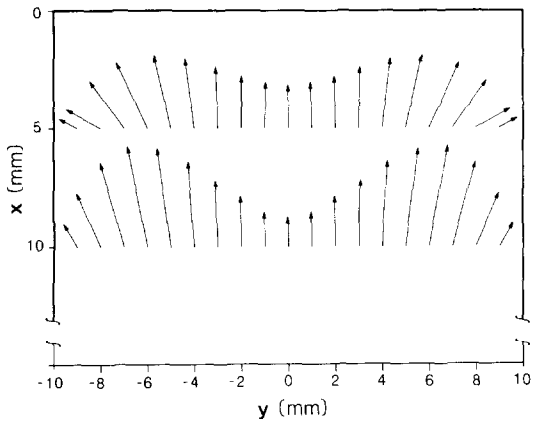

FIG. 13. v_x–v_y velocity field near cold thermode in horizontal plane $z = 12$ mm for $Ra = 8860$. Longest vector corresponds to 2.0 mm s^{-1}.

wall. This implies that flow reversal begins at larger values of x in planes $y \neq 0$. Hence, a velocity component $v_y \neq 0$ must exist in these planes.

3.6. *The flow near the cold end in the plane* $z = 12$ mm

The existence of a non-zero velocity component v_y was proven experimentally. We measured v_x and v_y in the plane $z = 12$ mm for $Ra = 8860$. The results, shown in Fig. 13, indicate a flow towards the side walls. For corresponding y-coordinates symmetric about $y = 0$, v_y is larger at $x = 5$ mm than at $x = 10$ mm. This 3-D flow reversal is shown in more detail in the following section.

3.7. *The velocity component* v_z *near the cold end in the plane* $z = r_0$

To characterize the fluid flow from the upper half of the cylinder into its lower half near the cold thermode, we measured the velocity component v_z in the plane $z = r_0$. The measurement locations were chosen to form a 1 mm by 1 mm x–y grid with the boundaries at 0 and 25 mm for x, and at -10 and 10 mm for y. If one imagines the velocity v_z measured at each grid-point to be represented by a vector perpendicular to the plane $z = r_0$, then all the ends of the 26×21 vectors (including the null vectors on the no-slip boundaries $x = 0$, $y = \pm 10$ mm) form a continuous surface. Oblique projections of this surface are shown for four different Ra's in Fig. 14. The same velocity scale was used for the four plots.

Now we can fully describe the 3-D flow reversal. Note that only fluid in the vicinity of the plane $y = 0$ flows along the thermode into the lower half of the cylinder. Fluid moving at larger $|y|$ towards the cold end diverts towards the side walls (see also Fig. 13) and then flows along those (Fig. 14) into the cylinder's lower half. There it recombines with the '2-D flow' to return to the hot end where the same partition occurs.

In comparing the four projections of Fig. 14 one obtains the following trends with increasing Ra:

(a) the flow velocities increase;

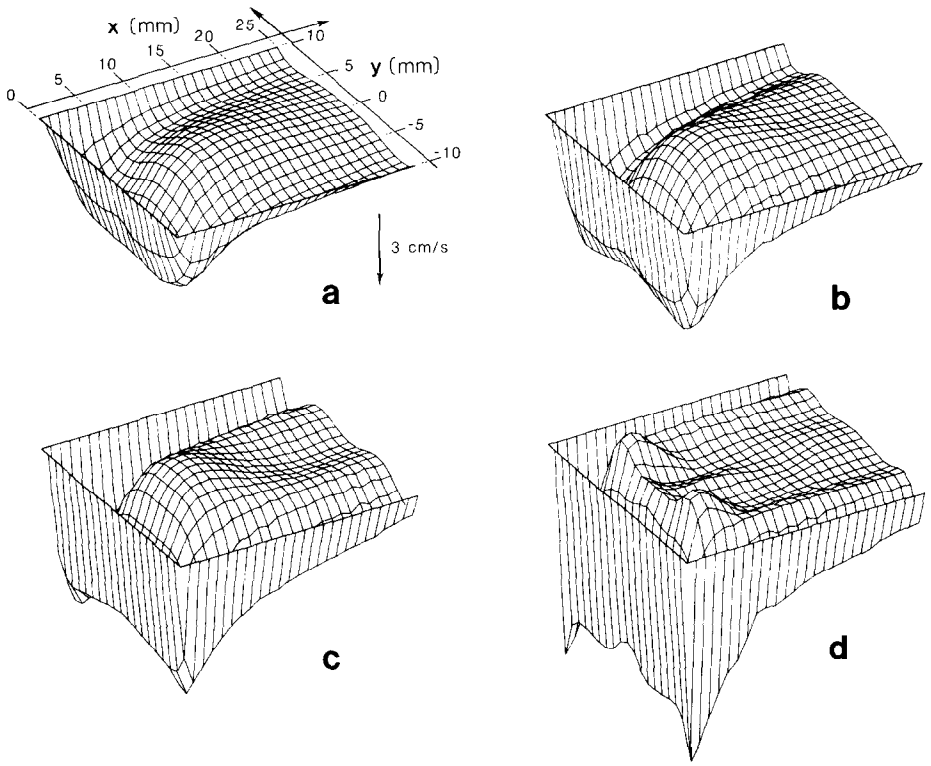

FIG. 14. Vertical velocity component v_z near cold thermode measured in the horizontal mid-plane ($z = 10$ mm) for (a) $Ra = 3580$, (b) $Ra = 8860$, (c) $Ra = 18\,700$, (d) $Ra = 342\,100$. Same velocity scale for all figures.

(b) the 'side wall flow' becomes more pronounced;
(c) boundary layers develop at both thermode and side wall;
(d) the location of maximum vertical velocity moves into the corners formed by thermode and side wall;
(e) two recirculation cells develop (see the 'bumps') that are symmetric and slanted with respect to the plane $y = 0$.

This 3-D flow reversal may seem somewhat complicated, but can be thermodynamically expected from the following thought experiment: if one were to suddenly thermally isolate the cylinder, then the fluid in the cylinder would keep convecting until the temperature at any boundary location would be the same. This means that there is not only a driving force to bring the two thermodes to a common temperature. In addition, the cylinder wall has to be brought to the same temperature. This can be achieved by the convective flow of warmer fluid along colder wall regions and vice versa. This side wall flow must obviously be strongest close to the thermodes. It will supposedly be less pronounced in the case of a less conducting wall. As, per definition, a fluid does not exchange heat with an adiabatic wall, one might conclude, that in this special case flow reversal occurs only along the thermodes. However, when the wall is highly conducting, the side wall flow extends far into the core-region, as shown in Fig. 14.

Acknowledgements—We thank Dr L. M. Fingerson of Thermo-Systems, Inc. for designing the optical frequency shifting technique for determining the flow direction. We are grateful to Prof. H. Riveros who suggested the radiation heating arrangement. A. C. Hurford helped with some of the measurements. The 3-D hidden-line plots were prepared with PLOT 79, developed by Dr Nelson Beebe at the University of Utah. His help in writing the programs is very much appreciated. Support of this research by the National Aeronautics and Space Administration under Grant NSF 1534 is also gratefully acknowledged.

REFERENCES

1. S. Ostrach, Natural convection in enclosures, *Adv. Heat Transfer* **8,** 161–227 (1972).
2. I. Catton, Natural convection in enclosures, *Proc. 6th Int. Heat Transfer Conf.*, Vol. 6, pp. 13–31 (1978).
3. G. H. Schiroky and F. Rosenberger, High Rayleigh number heat transfer in a horizontal cylinder with adiabatic wall, *Int. J. Heat Mass Transfer* **27,** 630–633 (1984).
4. S. W. Hong, Natural circulation in horizontal pipes, *Int. J. Heat Mass Transfer* **20,** 685–691 (1977).
5. F. Rosenberger, Fluid dynamics in crystal growth from vapors, *PhysicoChem. Hydrodyn.* **1,** 1–24 (1979).
6. A. Bejan and C. L. Tien, Fully developed natural counterflow in a long horizontal pipe with different end temperatures, *Int. J. Heat Mass Transfer* **21,** 701–708 (1978).
7. S. Kimura and A. Bejan, Numerical study of natural convection in a horizontal duct with different end-temperatures, *Wärme- und Stoffübertragung* **14,** 269–280 (1980).
8. T. H. Shih, Computer-extended series: natural convection in a long horizontal pipe with different end temperatures, *Int. J. Heat Mass Transfer* **24,** 1295–1303 (1981).
9. S. Kimura and A. Bejan, Experimental study of natural convection in a horizontal cylinder with different end temperatures, *Int. J. Heat Mass Transfer* **23,** 1117–1126 (1980).
10. F. Durst, A. Melling and J. H. Whitelaw, *Principles and Practice of Laser-Doppler Anemometry*. Academic Press, London (1976).
11. L. E. Drain, *The Laser Doppler Technique*. Wiley, Chichester (1980).
12. B. M. Watrasiewicz and M. J. Rudd, *Laser Doppler Measurements*. Butterworths, London (1976).
13. T. S. Durrani and C. A. Greated, *Laser Systems in Flow Measurement*. Plenum Press, New York (1977).
14. S. K. Friedlander, *Smoke, Dust, and Haze*. Wiley, New York (1977).
15. *Matheson Gas Data Book*, Matheson Gas Products, East Rutherford, New Jersey (1971).
16. S. Bretsznajder, *Prediction of Transport and Other Physical Properties of Fluids*. Pergamon Press, Oxford (1971).
17. R. B. Bird, W. E. Stewart and E. N. Lightfoot, *Transport Phenomena*. Wiley, New York (1960).
18. G. H. Schiroky, Free convection of gases in a horizontal cylinder with differentially heated end walls—a study by laser Doppler anemometry, Ph.D. dissertation, University of Utah, Salt Lake City, Utah (1982).
19. B. Roux, Personal communication (1982).
20. D. E. Cormack, L. G. Leal and J. Imberger, Natural convection in a shallow cavity with differentially heated end walls. Part 1. Asymptotic theory, *J. Fluid Mech.* **65,** 209–229 (1974).
21. D. E. Cormack, L. G. Leal and J. H. Seinfeld, Natural convection in a shallow cavity with differentially heated end walls. Part 2. Numerical solutions, *J. Fluid Mech.* **65,** 231–246 (1974).
22. J. Imberger, Natural convection in a shallow cavity with differentially heated end walls. Part 3. Experimental results, *J. Fluid Mech.* **65,** 247–260 (1974).
23. A. Bejan and C. L. Tien, Laminar natural convection heat transfer in a horizontal cavity with different end temperatures, *J. Heat Transfer* **100,** 641–647 (1978).
24. A. E. Gill, The boundary-layer regime for convection in a rectangular cavity, *J. Fluid Mech.* **26,** 515–536 (1966).
25. B. Roux, J. C. Grondin, P. Bontoux and B. Gilly, On a high-order accurate method for the numerical study of natural convection in a vertical square cavity, *Numerical Heat Transfer* **1,** 331–349 (1978).
26. R. S. Marshall, J. C. Heinrich and O. C. Zienkiewicz, Natural convection in a square enclosure by a finite-element, penalty function method using primitive fluid variables, *Numerical Heat Transfer* **1,** 315–330 (1978).
27. P. G. Simpkins and T. D. Dudderar, Convection in rectangular cavities with differentially heated end walls, *J. Fluid Mech.* **110,** 433–456 (1981).
28. C. Quon, Free convection in an enclosure revisited, *J. Heat Transfer* **99,** 340–342 (1977).
29. A. Bejan, Note on Gill's solution for free convection in a vertical enclosure, *J. Fluid Mech.* **90,** 561–568 (1979).
30. S. Ostrach, R. R. Loka and A. Kumar, Natural convection in low aspect ratio rectangular enclosures, in *Natural Convection in Enclosures-HTD* (edited by I. Catton and K. I. Torrance), Vol. 8, pp. 1–10. ASME, New York (1980).

CONVECTION NATURELLE DE GAZ DANS UN CYLINDRE HORIZONTAL AVEC DES EXTREMITES CHAUFFEES DIFFEREMMENT

Résumé—La convection naturelle de gaz dans un cylindre horizontal (rayon sur longueur, $r_0/L = 0{,}1$) avec des températures différentes aux extrémités et un gradient de température le long de la paroi est caratérisée par l'anémométrie laser Doppler. Des expériences sont conduites dans un large domaine de nombre de Rayleigh ($74 < Ra < 1{,}3 \times 10^6$ avec $Ra \propto r_0^3$), rendu variable à travers la nature et la pression du gaz. Dans le plan médian vertical, les profils de vitesse dans le coeur du cylindre à faible Ra, et dans la région d'extrémité à grand Ra, sont comme l'indique les modèles 2-D. Pour les régions d'extrémité néanmoins, on constate un comportement 3-D prononcé. On trouve que seule une partie du fluide se déplace le long de la thermode froide (chaude) vers la moitié inférieure (supérieure) de cylindre. La partie restante change la direction de l'écoulement en l'abaissant (l'élevant) à une distance considérable de la thermode respective.

DIE FREIE KONVEKTION VON GASEN IN EINEM HORIZONTALEN ZYLINDER MIT UNTERSCHIEDLICH BEHEIZTEN ENDEN

Zusammenfassung—Die freie Konvektionsströmung von Gasen in einem horizontalen Zylinder (Verhältnis Radius zu Länge $r_0/L = 0{,}1$) mit unterschiedlichen Endtemperaturen und einem linearen Temperaturgradienten an der Wand wurde mit Hilfe der Laser-Doppler-Anemometrie untersucht. Versuche wurden über einen weiten Bereich der Rayleigh-Zahl ($74 < Ra < 1{,}3 \times 10^6$, mit $Ra \sim r_0^3$) durchgeführt, wobei die Ra-Zahl über Gasvolumen und Gasdruck verändert wurde. In der vertikalen Mittelebene ergaben sich Geschwindigkeitsprofile in Mittelteil des Zylinders bei kleinen Ra-Zahlen und in den Endbereichnen bei großen Ra-Zahlen, wie sie aus 2D-Modellen zu erwarten waren. Im Endbereich wurden ausgeprägte 3D-Strömungen beobachtet. Es zeigte sich, daß nur ein Teil des Fluids entlang der kalten (warmen) Thermode in die untere (obere) Hälfte des Zylinders strömt. Der restliche Teil des Fluids wechselt die Strömungsrichtung, indem er an der Seitenwand—weit über die betreffende Thermode hinaus—abfällt (aufsteigt).

СВОБОДНО-КОНВЕКТИВНОЕ ТЕЧЕНИЕ ГАЗОВ В ГОРИЗОНТАЛЬНОМ ЦИЛИНДРЕ, ТОРЦЕВЫЕ СТЕНКИ КОТОРОГО НАГРЕТЫ ДО РАЗНОЙ ТЕМПЕРАТУРЫ

Аннотация—С помощью лазерного допплеровского анемометра проведено исследование свободно-конвективного течения газов в горизонтальном цилиндре (с отношением радиуса к длине, равном $r_0/L = 0{,}1$), торцевые стенки которого нагреты до разной температуры, а температура на стенке изменяется по линейному закону. Эксперименты охватывали широкий диапазон чисел Релея ($74 < Ra < 1{,}3 \times 10^6$ при $Ra \propto r_0^3$), которые изменялись в зависимости от вида газа и его давления. В вертикальном центральном сечении профили скорости в ядре при малых значениях числа Ra и на периферии при высоких значениях Ra оказались аналогичными тем, которые рассчитываются с помощью двумерных моделей. Однако, в концевых областях наблюдалось ярко выраженное трехмерное течение. Обнаружено, что только часть жидкости протекает вдоль холодного (горячего) термода в нижнюю (верхнюю) половину цилиндра. Оставшаяся часть изменяет направление потока на боковой стенке на значительном расстоянии от соответствующего термода.